INVESTIGATION OF FRICTION STIR SPOT WELDING PARAMETERS ON SHEAR FORCE AND MICROHARDNESS OF AA 6061 AND PURE COPPER JOINTS

A. M. Hanafy [1*], H.A. Abdel-Aleem [2], A. M. Gaafer [3], E. H. Mansour [3]

[1] Mechanical Engineering Department, Higher Technological Institute, 6th of October, Giza, Egypt,

[2] Welding and Inspection Department, Central Metallurgical Research Institute (CMRDI), Cairo, Egypt,

[3] Mechanical Engineering Department, Faculty of engineering at Shoubra, Benha University, Shoubra, Cairo, Egypt.

*Correspondence: amr.hanafy@hti.edu.eg

ABSTRACT

Friction stir spot welding (FSSW) is widely utilized in this study for the purpose of joining dissimilar metals, specifically AA6061-T6 Aluminium Alloy and pure Copper. The parameters governing the welding process encompass tool speed, plunge depth, and dwell time. The study further delineates certain mechanical properties derived from the tensile-shear experiments of the AA6061-pure copper joints. Six welded specimens are performed at each process condition. Scanning electron microscopy (SEM) was used for the microstructure analysis. Energy Dispersive X-ray Spectroscopy (EDX) was used to analyze the elemental composition and distribution within the welded specimens. The maximum tensile shear force of 4.18 kN is achieved at 2000 rpm, 0.2 mm depth, and 20 seconds. Conversely, the minimum tensile shear force of 2.01 kN is obtained at 2200 rpm, 0.1 mm depth, and 15 seconds. The highest Microhardness value of the Stirred Zone (SZ) is 122.78 HV at 2200 rpm, 0.2 mm depth, and 15 seconds. In contrast, the lowest Microhardness value of 54.1 HV is recorded at 2000 rpm, 0.2 mm depth, and 15 seconds. The tensile shear force increases from 2.46 kN (conventional FSSW) to 2.64 kN (Stitch FSSW at 2 mm distance traveled) and 2.68 kN (Stitch FSSW at 4 mm distance traveled).

KEYWORDS: Friction stir spot welding, Aluminum Alloys, Pure Copper, Tensile Shear Load.

دراسة تأثير معايير اللحام بالاحتكاك والتقليب الموضعي على قوة القص والصلادة الدقيقة لوصلات سبيكة الألومنيوم 6061 والنحاس النقي

عمرو محمد حنفي محمود [1*]، حامد أحمد عبد العليم[2]، أحمد محمد جعفر[3]، السيد حمزة منصور[3]

[1] قسم الهندسة الميكانيكية، المعهد التكنولوجي العالي، السادس من اكتوبر، الجيزة، مصر.
[2] قسم اللحام والتفتيش، مركز بحوث الفلزات، القاهرة، مصر.
[3] قسم الهندسة الميكانيكية، كلية الهندسة بشبرا، جامعة بنها، القاهرة، مصر

*البريد الاليكتروني للباحث الرئيسي : amr.hanafy@hti.edu.eg

INVESTIGATION OF FRICTION STIR SPOT WELDING PARAMETERS ON SHEAR FORCE AND MICROHARDNESS OF
AA 6061 AND PURE COPPER JOINTS

الملخص

تُستخدم اللحام النقطي بالاحتكاك والتحريك (FSSW) على نطاق واسع في هذه الدراسة لغرض ربط المعادن غير المتشابهة، وتحديدًا سبيكة الألومنيوم AA6061-T6 والنحاس الخالص. تشمل المعلمات التي تحكم عملية اللحام سرعة الأداة وعمق الانغماس ووقت الانتظار. وتوضح الدراسة أيضًا بعض الخصائص الميكانيكية المستمدة من تجارب الشد والقص لمفاصل النحاس الخالص AA6061. يتم إجراء ست عينات ملحومة في كل حالة عملية. تم استخدام المجهر الإلكتروني الماسح (SEM) لتحليل البنية الدقيقة. تم استخدام مطيافية الأشعة السينية المشتتة للطاقة (EDX) لتحليل التركيب العنصري والتوزيع داخل العينات الملحومة. يتم تحقيق أقصى قوة قص شد تبلغ 4.18 كيلو نيوتن عند 2000 دورة في الدقيقة وعمق 0.2 مم و20 ثانية. وعلى العكس من ذلك، يتم الحصول على الحد الأدنى لقوة القص الشد 2.01 كيلو نيوتن عند 2200 دورة في الدقيقة، وعمق 0.1 مم، و15 ثانية. أعلى قيمة صلابة دقيقة لمنطقة التحريك (SZ) هي HV 122.78 عند 2200 دورة في الدقيقة، وعمق 0.2 مم، و15 ثانية. في المقابل، تم تسجيل أقل قيمة صلابة دقيقة HV 54.1 عند 2000 دورة في الدقيقة، وعمق 0.2 مم، و15 ثانية. تزداد قوة القص الشد من 2.46 كيلو نيوتن (FSSW التقليدية) إلى 2.64 كيلو نيوتن (Stitch FSSW عند مسافة 2 مم مقطوعة) و2.68 كيلو نيوتن (Stitch FSSW عند مسافة 4 مم مقطوعة).

الكلمات المفتاحية : اللحام بالاحتكاك والتقليب الموضعي، سبائك الألومنيوم، النحاس النقي، حمولة الشد القصوى.

1. INTRODUCTION

A common solid-state welding method for fusing sheet metals including copper, magnesium, and aluminum is FSSW. The substantial rotation of the tool with a shoulder and occasionally a pin combined with the downward movement causes friction between the tool's and the workpiece's surfaces, which causes the workpiece to deform plastically and generates a significant amount of heat in that particular area. The heat generated between the overlapping sheets ultimately causes the material of the workpiece next to the region of contact with the tool and sheet to soften, creating a strong bond between them. Studies have shown that critical welding parameters that affect the microstructure and properties of the joint include the tool's rotation speed, the rate at which the tool plunges, the length of the dwell, and the depth of the plunges among other factors [1-7].

The joining of different materials is becoming increasingly prevalent in businesses in order to acquire both technical and economic advantages [8-11]. However, the fusion joining of Al alloy to copper poses a crucial challenge due to the formation of thick and continuous intermetallic compounds (IMCs) [12, 13]. Various mechanical joining methods, such as self-piercing riveting, may lead to suboptimal working conditions, reduced efficiency, and an increase in structural weight [14]. It is noteworthy that solid phase joining techniques like explosive welding [15], ultrasonic welding [16], friction welding [17], friction stir welding (FSW) [18–22], and conventional FSSW offer viable options for joining dissimilar metals [23]. These approaches have the advantage of modifying issues commonly associated with fusion welding, such as solidification, liquation cracking, and porosity.

Aluminum Alloys such as AA6061-T6 and various Commercial Copper Alloys have been extensively utilized in the aviation and automotive industries, due to their exceptional strength, superior resistance to corrosion, favorable formability, and convenient machinability. Nevertheless, these alloys pose significant challenges in both design and welding due to the substantial difference in melting points between aluminum and copper, which restricts the application of traditional fusion welding techniques. Consequently, dissimilar joints are manufactured through the method of riveting, a process that necessitates specialized tools, supplementary fixtures, and a skilled workforce, and results in an increase in the overall weight of the joints. The utilization of FSSW

has been employed for the purpose of bonding aluminum to aluminum, aluminum to magnesium, aluminum to copper, and aluminum to carbon steel [24-31].

The use of FSSW has been widely applied in the manufacturing of automobile body panels, demonstrating efficiency in welding aluminum and copper components within aluminum vehicle structures [32-35].

The present work aims to study the effect of FSSW parameters on shear load and microhardness of lap joints between dissimilar materials to identify the optimized welding conditions that achieve the optimum values in these properties. An adjusted stitch FSSW technique is utilized to enhance the quality of joints between AA 6061 aluminum and pure copper.

2. Experimental Work

The materials used in this investigation are 6061 Aluminum alloy and pure copper plates. The aluminum plate is cut into a dimension of 25mm x 100mm x 2.2mm, While the copper plate is cut into a dimension of 25mm x 100mm x 1.4mm as exhibited in **Fig .1**. The chemical compositions of AA6061 and pure copper are listed in **Table 1.** The necessary size is measured and cleaned for the sheets that need to be welded. The 25 mm overlap gap is positioned toward the placement of the lap weld. Tool Material is from H13 Hot worked tool steel, which has a shoulder diameter of 10 mm, a pin diameter of 4 mm and a pin length of 3.2mm as shown in **Fig .2**. The benefits of H13 steel include high toughness, fatigue resistance, and suitability for hot working processes. The mechanical properties of AA6061, pure copper and H13 material are presented in **Table 2**. The Chemical Composition of H13 material is listed in **Table 3**.
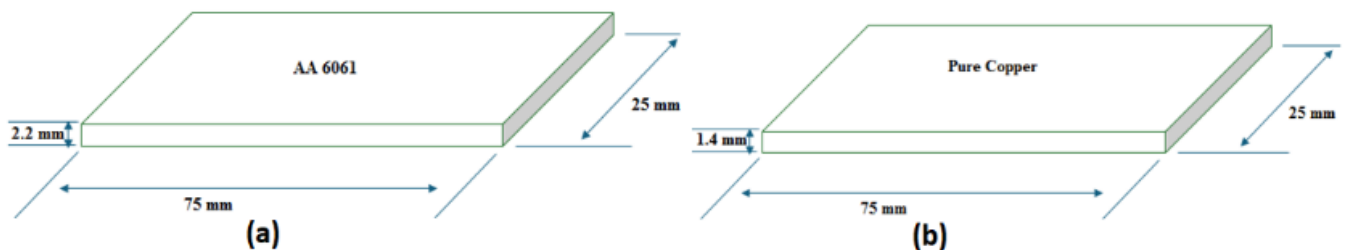

Fig. 1. Schematic drawing of (a) AA 6061 aluminum alloy (b) pure copper plates dimensions.

Table 1. Chemical composition of AA 6061 and pure copper plates [36].

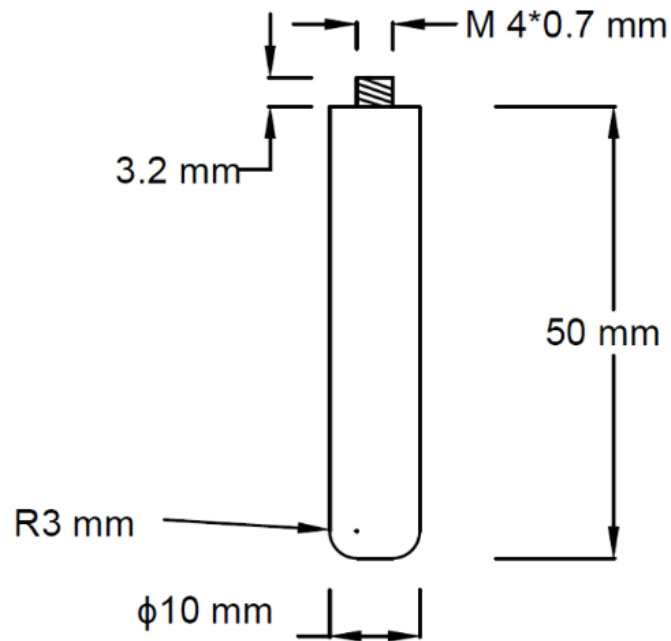| Material	Cu	Al	Zn	Ti	Fe	Mn	Si	Mg
Pure Copper	99.9	-	0.01	0.01	0.02	-	-	-
AA 6061	0.15	95.8	0.25	0.15	0.7	0.33	0.53	0.69

Fig. 2. Tool dimensions.

Table 2. Mechanical properties of AA 6061, pure copper plates and H13 material [37-39]**.**

Material	AA 6061	Pure Copper	H13 Tool Steel
Tensile strength, Mpa	260	232	1955
Yield strength, MPa	206	87	1560
Hardness	67 Hv	42 Hv	653 Hv

Table 3. Chemical composition of H13 tool material [40].

Element	C	Si	Mn	P	S	Cr	Mo	V
wt %	0.38	0.97	0.34	0.02	0.002	5	1.34	0.93

The process parameters include rotation speed, dwell time, and plunge depth with respective values of (1800-2000-2200) rpm, (10-15-20)sec, and (Zero-0.1-0.2)m. The influence of the characteristics of the formed joint (microhardness, and lap shear strength) is studied. The workpiece was securely clamped on a Fixture from steel 37 backing plate with dimensions of 380 $\times$ 255 $\times$ 10 mm^3 to ensure that the material withstands the significant perpendicular and lateral forces developed during the process as shown in **Fig .3**. Another advantage of the fixture is to dissipate the heat generated from the welding process.
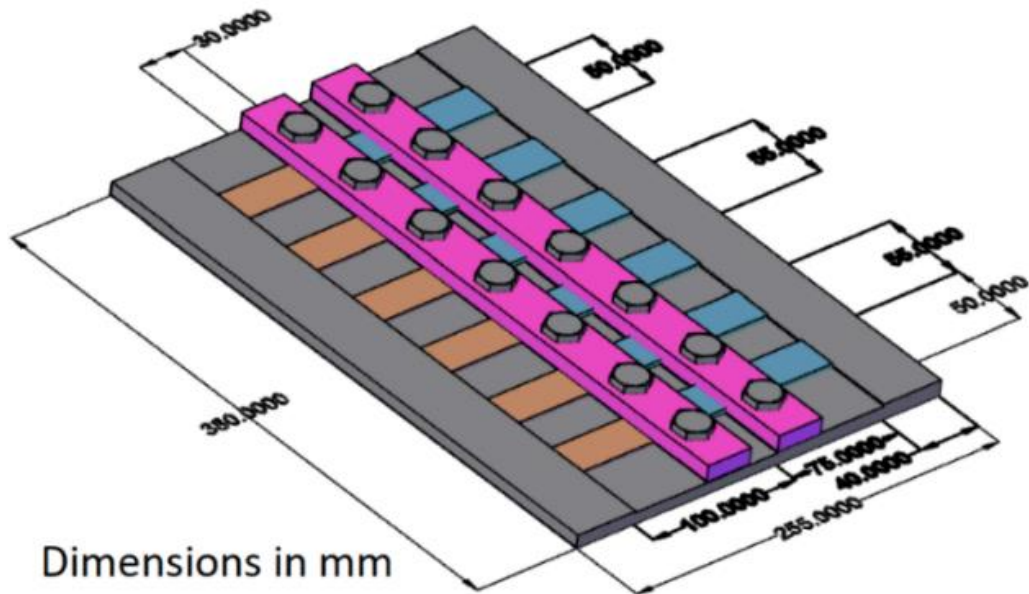
Fig. 3. Fixture dimensions of process.

The welding experiments are conducted via CNC Automatic Machine at different welding parameters. Vertical plunge rate of 150 mm/min is applied during the insertion of the tool in the overlapped plates. The Aluminum plate is placed on the upper side and the copper plate is placed on the bottom side of the process due to lower thermal conductivity of Aluminum plate that produced sufficient heat for better mixing of the joint [41-42]. **Fig. 4** presents the position of welded plates. Six repetitions of each welding condition are conducted.
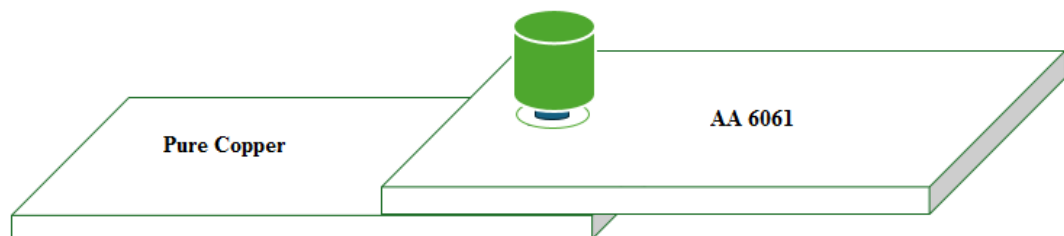

Fig. 4. The position of AA 6061 aluminum and pure copper plates in FSSW process.

At a tool speed of 2000 rpm and a plunge depth of 0.2 mm, a modified form of FSSW is conducted. The Stitch FSSW technique is implemented to enhance the area of the weld. The tool penetrates the overlapped materials, initiating a first dwell period of 0.6 seconds, followed by a horizontal traversal of (2-4) mm. Subsequently, a second dwell time of 0.9 seconds is observed before the tool retracts vertically from the joint.

The performance of the joints has been evaluated using the tensile-shear test. The experiments on tensile shear were executed utilizing specimens of specified dimensions according to ISO 14273:2016 [43], as illustrated in **Fig. 5**. The experimentation is conducted under a consistent cross head speed of 1 mm/min. Two shims plates are supported the upper and lower plates during the tensile shear test as shown in **Fig. 6**.
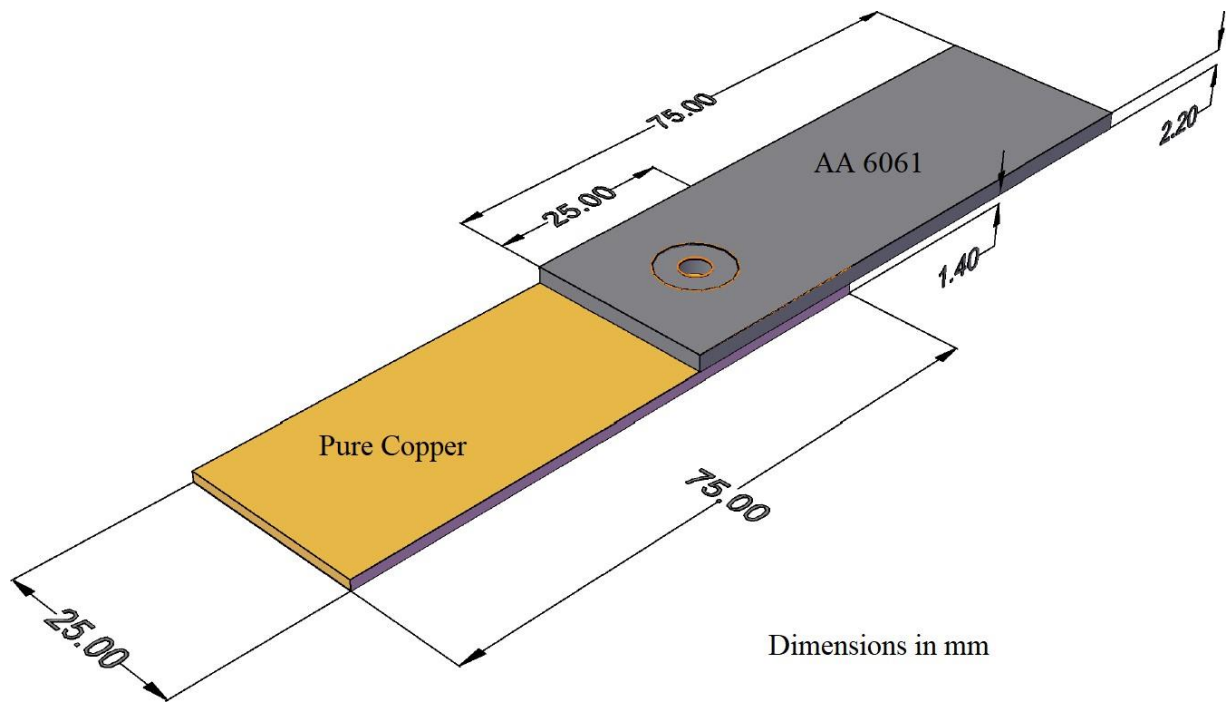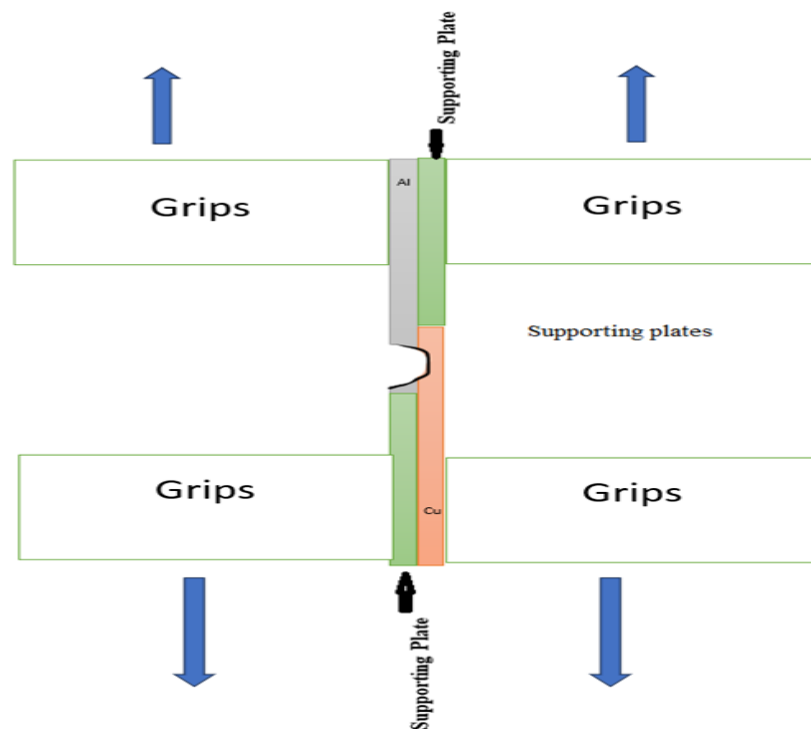
Fig. 5. Tensile test specimen.

Fig. 6. Tensile test machine at room temperature.

The specimens are cut transversely to the weld location using a CNC wire cutting machine. Subsequently, the samples were sectioned by an electrical discharge cutting machine for the purpose of conducting macrostructure and microstructure analysis, to the specified dimensions of (25 mm width x 12.5 mm length x 3.6 mm thickness). Using (SiC) paper, specimens for metallographic examination are made by wet grinding in various grits (800, 1000, and 1200). The final polishing is done using the diamond compound (1 m particle size) from the disc-polishing machine. The specimens are etched using Keller's reagent to reveal the microstructure.

Vickers microhardness profile of stirred zone was measured on the cross section perpendicular to the processing direction using a Vickers indenter with 490 mN load for 10 s. Microhardness distribution is measured in the middle of specimen. The microhardness measurements are carried out every 0.5 mm. The microhardness measurements are conducted on specimens prepared for metallographic examination. **Fig. 7** shows the preparation and the measurement of Microhardness weld specimen. SEM is used to investigate the fracture morphologies of weld specimens. EDX is an x-ray technique used to identify the elemental analysis of welded joints.
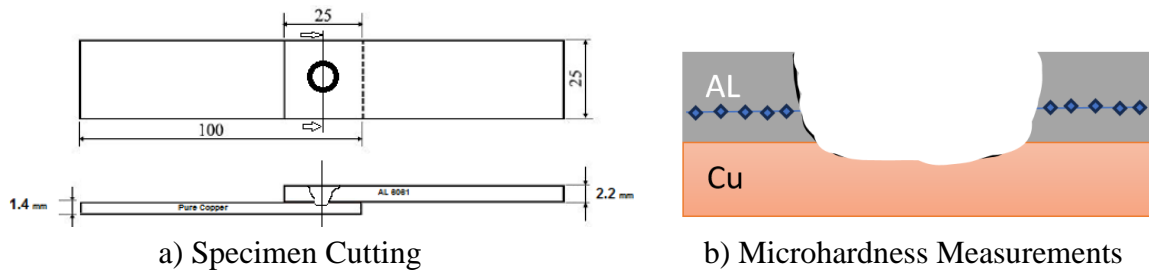

a) Specimen Cutting   b) Microhardness Measurements

Fig. 7. The preparation and the measurement of microhardness weld specimen

3. Results and Discussions

3.1. Effect of dwell time

Fig. 8 illustrates the Macrostructure, upper and lower sides of welded plates at 1800 rpm -Zero mm plunge depth with (10-15-20) sec dwell time. The graph shows a good mixing area in the three cases. It is noticed that some excess flash of welded material in the upper side of the Al side. The material in the weld zone is subjected to higher temperatures and a longer duration of mechanical stirring, which enhances the plasticity of the materials of AA 6061 and pure Cu.
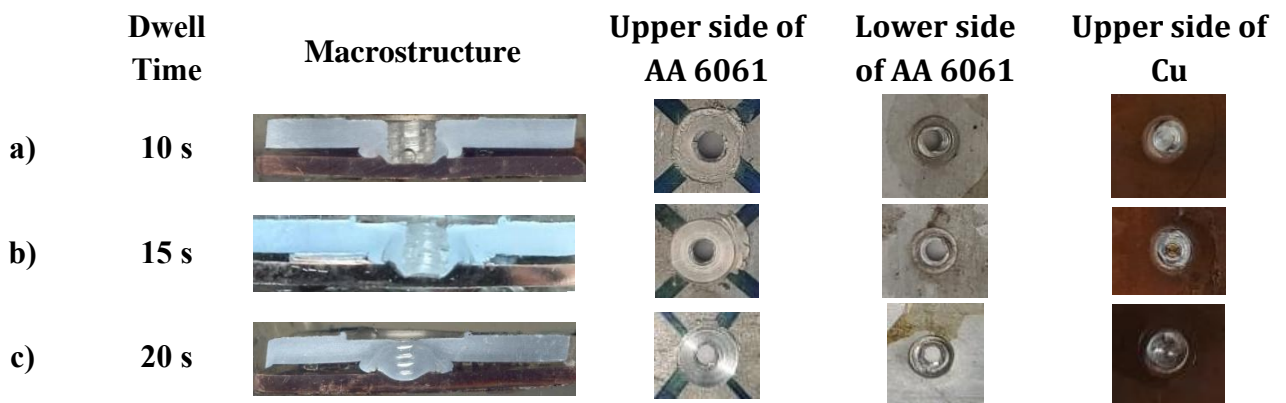
	Dwell Time	Macrostructure	Upper side of AA 6061	Lower side of AA 6061	Upper side of Cu
a)	10 s				
b)	15 s				
c)	20 s				

Fig. 8. Influence of dwell time on welded specimen at 1800 rpm -zero mm plunge depth macrostructure, upper and lower part plates at a) 10 sec b) 15sec c) 20 sec .
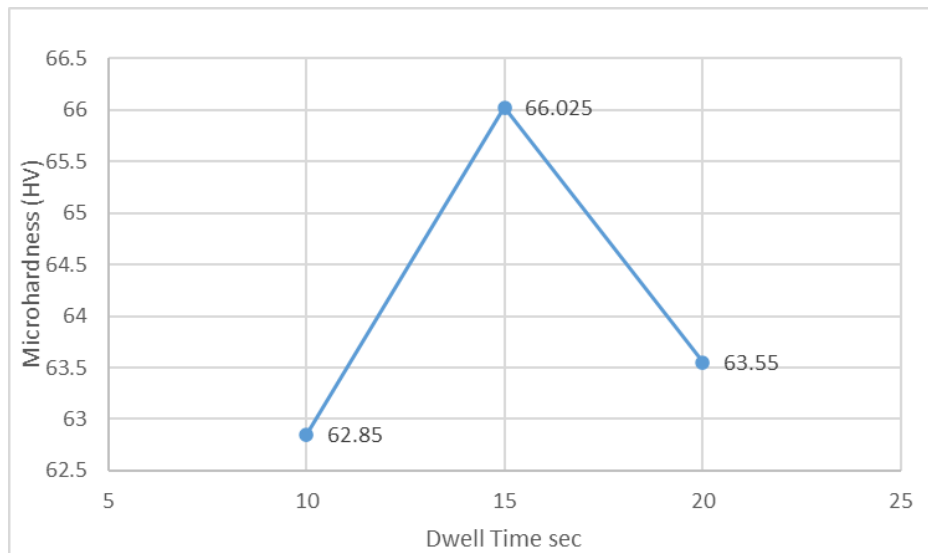
Fig. 9. Effect of dwell time on microhardness of sz at 1800 rpm- zero mm plunge depth**.**

The microhardness results of 1800 rpm -zero plunge depth welded joint are recorded. The microhardness of SZ slightly increases from 62.85 Hv at 10 sec dwell time to 66.02 Hv at 15s, Then it decreases to 63.55 Hv at 20 sec dwell time as shown in **Fig. 9**. At a shorter dwell time of 10 seconds, the material does not receive sufficient heat and time to fully develop a refined microstructure, resulting in a relatively lower hardness. As the dwell time increases to 15 seconds, the material undergoes more significant plastic deformation and recrystallization due to the extended exposure to heat and mechanical stirring, leading to a peak in hardness at 66.02 HV. However, with a further increase in dwell time to 20 seconds, the material may experience overheating and grain growth, which can reduce the overall hardness. Additionally, the prolonged thermal exposure might lead to a reduction in the dislocation density or potential softening of the material, causing the hardness to decrease to 63.55 HV. At 1800 rpm and zero plunge depth, an observation is made indicating that the tensile shear force exhibits an initial increase with dwell time ranging from 10 to 15 seconds, followed by a subsequent decrease upon the dwell time reaching 20 seconds, as depicted in **Fig.10.** The shear force rises from 2.28 kN to 3.60 kN, indicating an enhancement in the joint's strength. This increase can be attributed to better material intermixing and more efficient bonding due to the prolonged exposure to heat and mechanical action at 15 seconds. However, as the dwell time further increases to 20 seconds, the shear force decreases to 3.15 kN. This reduction may be caused by excessive heat input and material softening, which could weaken the joint. The longer dwell time may also lead to grain coarsening or potential defects such as voids or inclusions within the weld zone, thereby reducing the joint's mechanical strength.
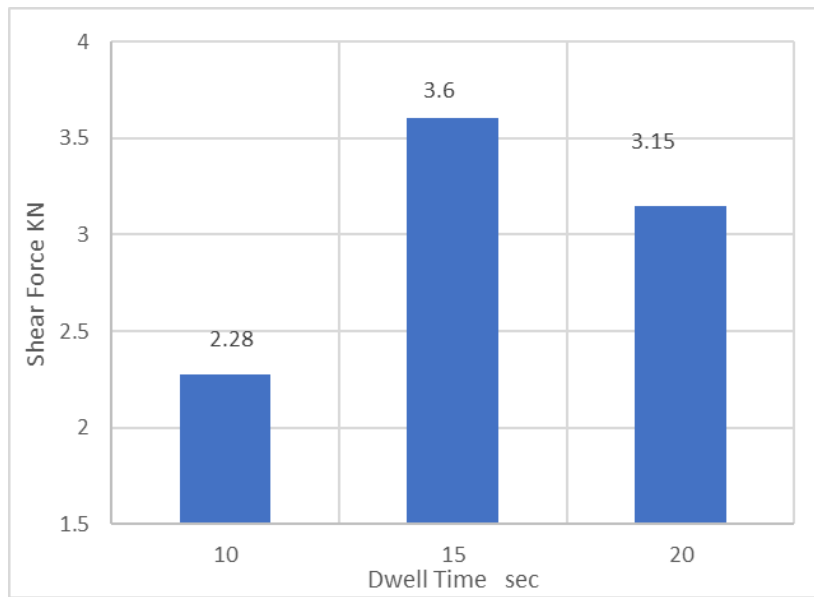
Fig. 10. Effect of dwell time on Shear Force at 1800 rpm- zero mm Plunge Depth.

3.2 Effect of rotational speed

Fig. 11 illustrates the Macrostructure, upper and lower sides of Welded plates at 10 sec dwell time -0.1 mm plunge Depth with 1800-2000-2200 rpm rotational speed. The graph shows the perfect mixing area at the case of 2200 rpm. The top view of the Al side of the spot-welded joints shows that the extruded material flashing to the sides of the shoulder projection is nearly uniform. The excess flashes occurred due to excessive heat generation because of the higher rotational speed.
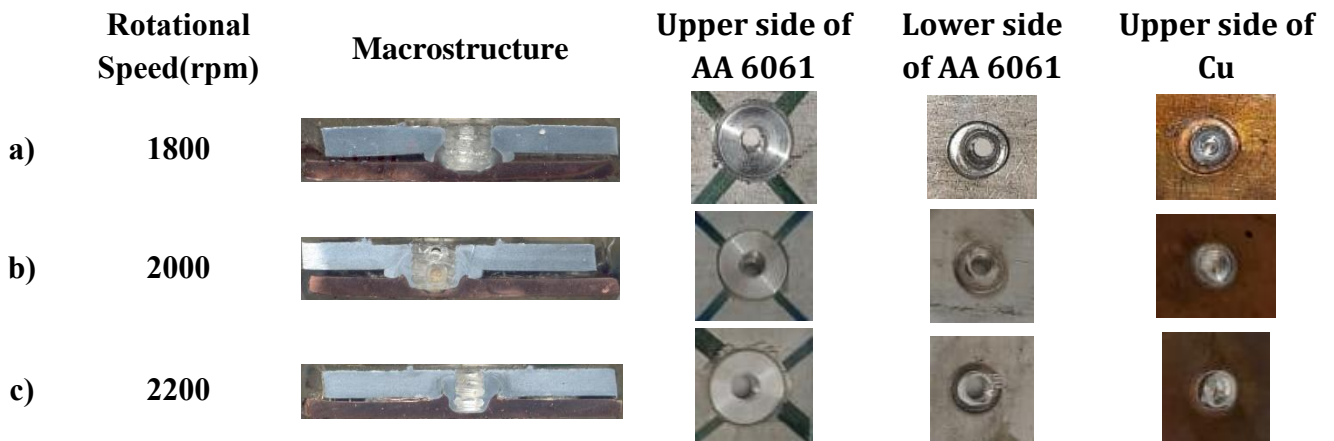
	Rotational Speed(rpm)	Macrostructure	Upper side of AA 6061	Lower side of AA 6061	Upper side of Cu
a)	1800				
b)	2000				
c)	2200				

Fig. 11. Influence of rotational speed on welded specimen at 10s dwell time- 0.1 mm plunge depth macrostructure, upper- and lower-part plates at a) 1800 b) 2000 c) 2200 (rpm)**.**

As the rotating speed changes, so does the shear force. As seen in **Fig. 12**, the shear force increases with rotational speed up to a certain point, specifically at 2000 rpm, where it reaches a peak of 2.98 kN. However, beyond this speed, at 2200 rpm, the shear force declines to 2.7 kN. This behavior occurs under a 10-second dwell time and a 0.1 mm plunge depth. This pattern suggests that up to 2000 rpm, the increase in rotational speed enhances the material mixing and bonding in the weld, resulting in a stronger joint and higher shear force. However, as the rotational speed

exceeds 2000 rpm, the excessive heat generated may cause adverse effects, such as weakening of the material due to overheating or other structural changes, leading to a reduction in shear strength. This indicates that there is an optimal rotational speed (around 2000 rpm) for maximizing the shear force under these specific welding conditions. The microhardness of the SZ in a welded specimen varies with the rotational speed at a constant dwell time of 10 seconds and a plunge depth of 0.1 mm as shown in **Fig. 13** At 1800 rpm, the microhardness is high at 76.425 HV, suggesting that the generated heat is sufficient for effective material mixing and recrystallization, resulting in a harder stir zone. When the rotational speed increases to 2000 rpm, the microhardness drops to 68.3 HV, likely due to excessive heat causing grain growth or other microstructural changes that reduce hardness. As the rotational speed increases to 2200 rpm, the microhardness rises to 72.825 HV. This suggests that the higher speed, along with specific welding conditions like dwell time and plunge depth, may improve the microstructure through enhanced material flow or more efficient heat distribution, resulting in greater hardness compared to the 2000 rpm condition. Chu et al. [44] reported that the material flow behavior becomes unstable at shorter dwelling times. The shear force varies with changes in rotational speed. As rotational speed increases from 1800 rpm to 2000 rpm, the shear force rises from 2.4 KN to 2.98 KN. This increase is due to improved heat generation and material mixing, leading to a stronger weld. However, when the rotational speed is further increased to 2200 rpm, the shear load decreases to 2.7 KN. This reduction is likely caused by excessive heat, which can result in defects such as voids or material degradation, thereby weakening the weld.
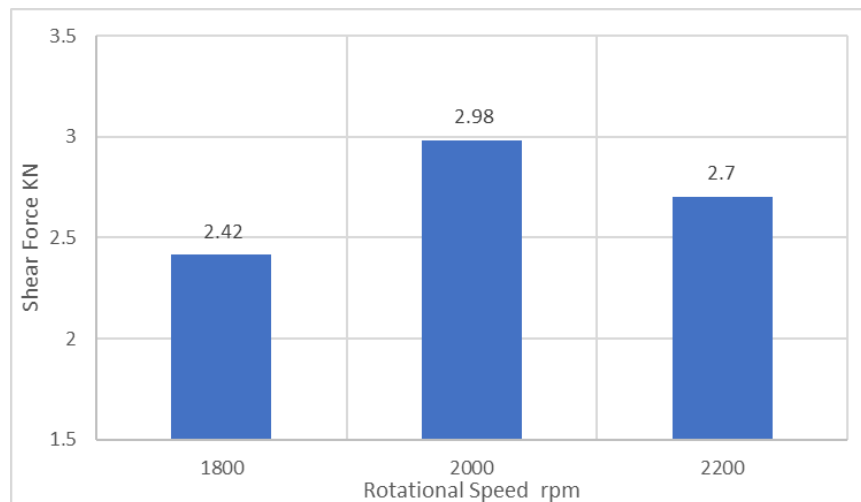

Fig. 12. Effect of rotational speed on shear force at 10 sec dwell time- 0.1 mm plunge depth.
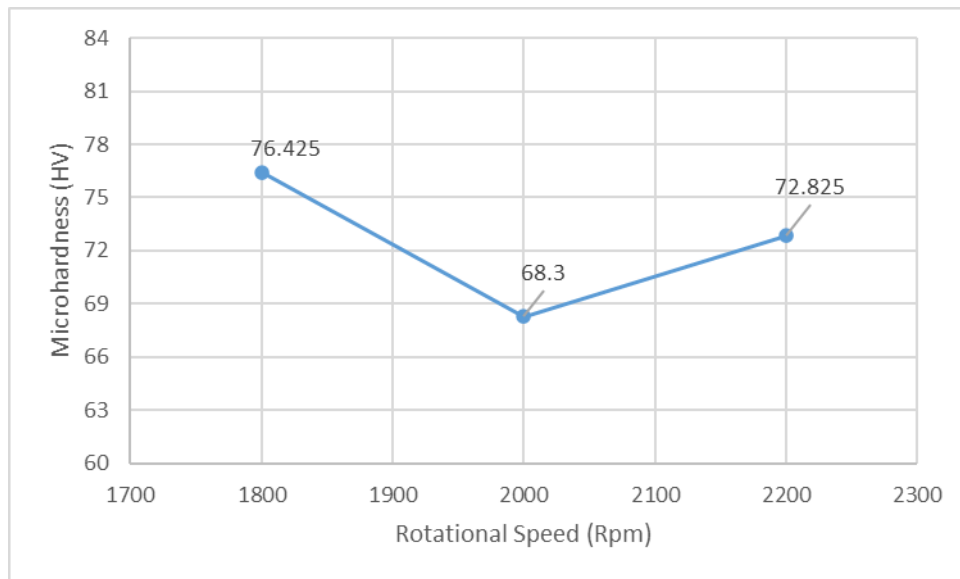
Fig. 13. Effect of rotational speed on microhardness of sz at 10 sec dwell time- 0.1 mm plunge depth.

3.3 Effect of plunge depth

Fig. 14. exhibits the Macrostructure, upper and lower sides of welded plates at 2000 rpm - 15 sec dwell time with zero-0.1-0.2 mm plunge depth. The graph illustrates a good mixing area in the case of 0.2 mm. Some excess flash of material appears in the upper side of the Al side increasing gradually from zero to 0.1- and 0.2-mm plunge depth. The mode of fracture of an eyelet appears on the upper side of Cu. Excessive flashes were generated due to an increased penetration depth, which was caused by the higher downward force. Circular indentations formed by the shoulder projection are visible under various applied parameters [45].
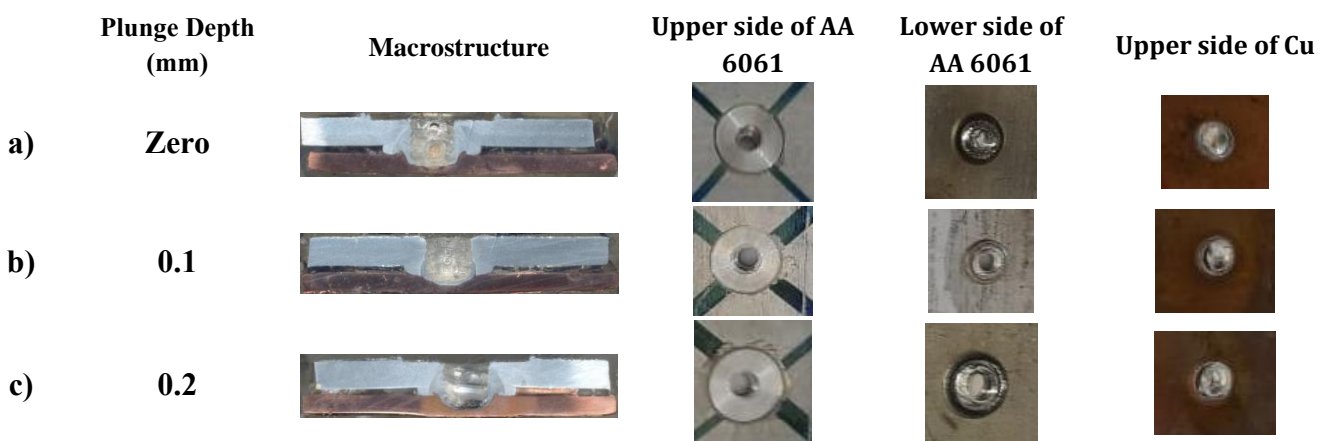

Fig. 14. Influence of Plunge Depth on Welded Specimen at 2000 rpm – 15 sec Dwell time Macrostructure, upper- and lower-part plates at a) Zero b) 0.1 c) 0.2 (mm).

The value of microhardness increases from 88 Hv to 95.8 Hv when the plunge depth increases. This increase suggests that a greater plunge depth improves the material bonding and leads to a more refined microstructure, resulting in higher hardness. Then it decreases to 54.1 Hv with increasing the plunge rate to 0.2 mm due to excessive heat input at the higher plunge depth. The additional heat can lead to grain growth, material softening, or even microstructural

degradation, which negatively impacts the hardness of the material as illustrated in **Fig. 15**. The
effect of plunge depth on the shear force at a rotational speed of 2000 rpm and a dwell time of 15
seconds. As the plunge depth increases, the shear lap force also rises. Specifically, the shear force
increases from 2.11 kN at a plunge depth of 0 mm to 2.26 kN at a plunge depth of 0.1 mm, and
further to 2.5 kN at a plunge depth of 0.2 mm. as shown in **Fig. 16**. When the plunge depth
increases, the material engagement between the tool and the workpieces is improved, leading to
better bonding and increased shear strength of the joint. The higher plunge depth allows for more
material to be plastically deformed and stirred, resulting in a stronger weld with a higher shear
force. This behavior is consistent with the idea that increasing the plunge depth enhances the
mechanical interlocking and bonding between the materials, thereby increasing the shear lap force.
Piccini et al. [46] investigated the effect of plunging depth in the FSSW process and examined the
impact of altering the position of alloys in superimposed joints when welding AA5052 and AA6063
sheet specimens. They discovered that increasing the tool plunging depth led to higher fracture
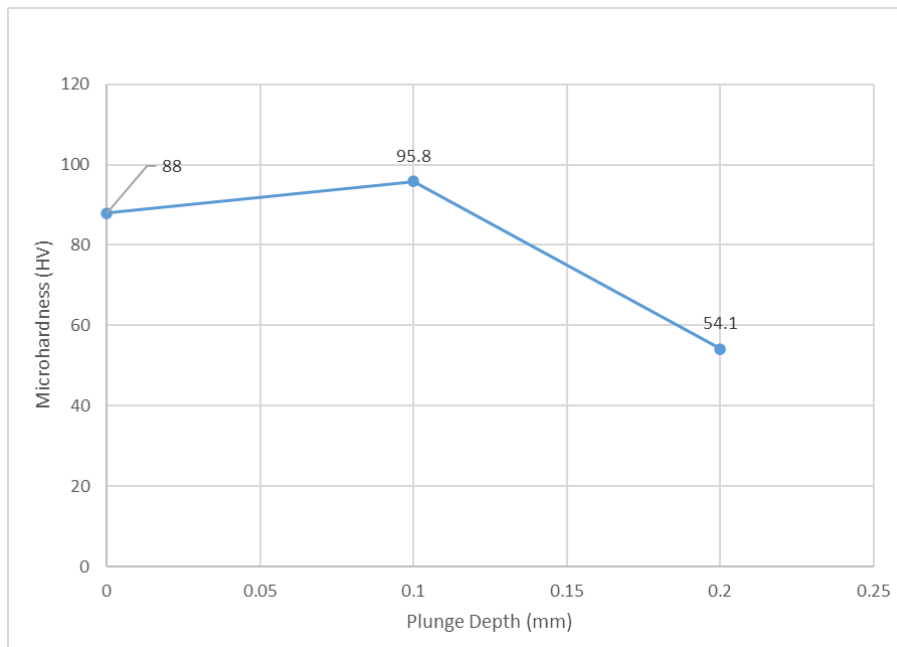loads in both alloy configurations.

Fig. 15. Effect of plunge depth on the microhardness of SZ at at 2000 rpm- 15 sec dwell
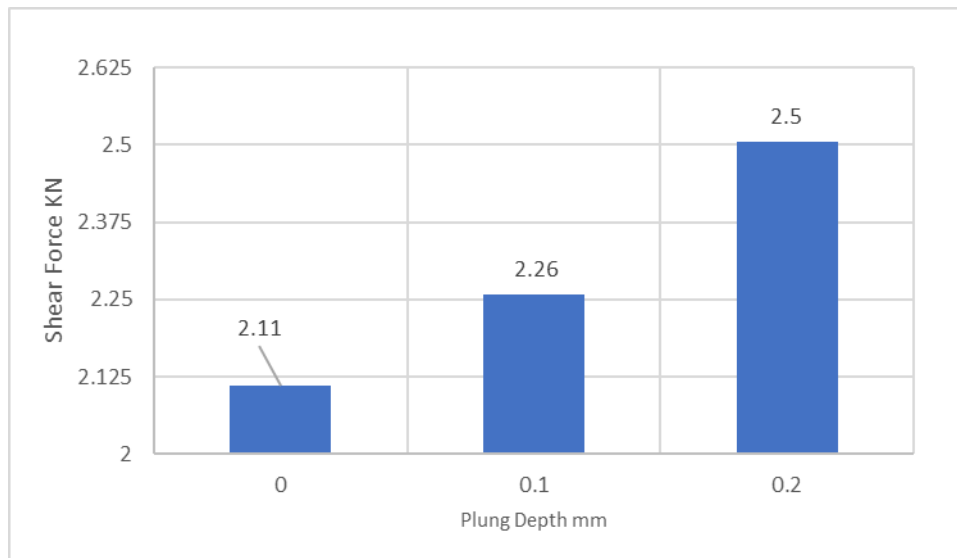time.

Fig. 16. Effect of plunge on the shear force at 2000 rpm- 15 sec dwell time.

3.4 Stitch FSSW investigation

Fig. 17. illustrates various weld joints produced using the conventional FSSW technique and the Stitch FSSW technique, each with a travel distance ranging from 2 to 4 mm. The results indicate that, under the conditions of 2200 rpm tool speed and 0.2 mm plunge depth, the tensile shear force exhibits an increase from 2.46 kN for traditional FSSW to 2.64 kN for Stitch FSSW at a travel distance of 2 mm, and further to 2.68 kN for Stitch FSSW at a travel distance of 4 mm. The lack of penetration defect observed in specimen condition 4 - number 3 (A4-3) and condition 4-number 6 (A4-6) is attributed to the low plunge depth, which resulted from vibrations of the rotational tool in the CNC machine. Additionally, the excessive flashes were caused by the generation of excessive heat due to the higher rotational speed. **Fig. 18** illustrates the Macro-Structure of the specimen subjected to a rotational speed of 2200 rpm and a plunge depth of 0.2 mm. This includes **Fig. 18 (a)** shows the conventional Friction Stir Spot Welding (FSSW), **Fig. 18 (b)** presents the Stitch FSSW with a 2 mm weld distance, and **Fig. 18 (c)** exhibits the Stitch FSSW with a 4 mm weld distance. An observation reveals a correlation between the increased weld distance and its impact on the strength of the weld joint. Walz et al. [47] examined the impact of stitch seam length on the strength of intersecting friction stir welds in EN AW-6016 T4 sheets. They found that tensile and fatigue strength improve with increased stitch length, with 15 mm stitches achieving 87% of the tensile strength and 50% of the plastic elongation of the base material. Shorter welds reach 67% of the tensile strength due to reduced hardness from high cyclic heat input, while the substitute proof strength remains unaffected. Ding et al. [48] reported that various FSSW process variants, including conventional FSSW, pinless FSSW, refill FSSW, and short traverse techniques like swept FSW, stitch FSW, and swing FSW, have been studied with a focus on heat generation, material flow, parameter optimization, microstructural evolution, and mechanical properties.
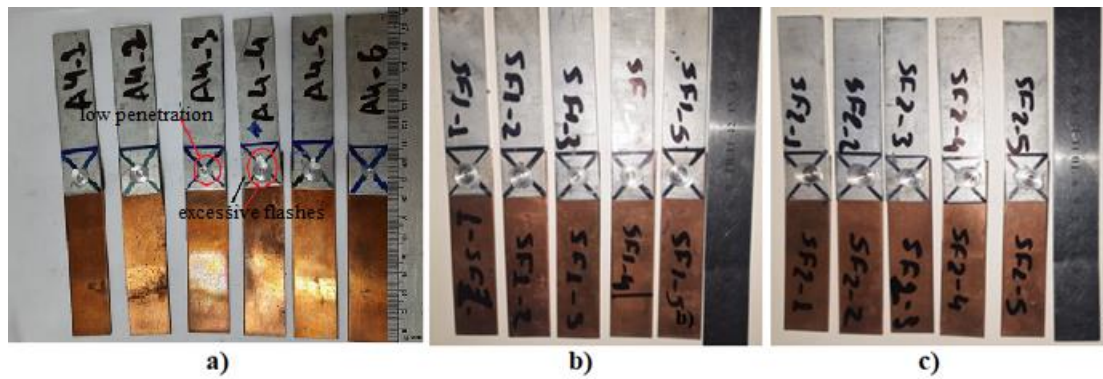
Fig. 17. AA 6061 -pure copper lap jointed for a) traditional fssw b) stitch fssw for 2mm distance
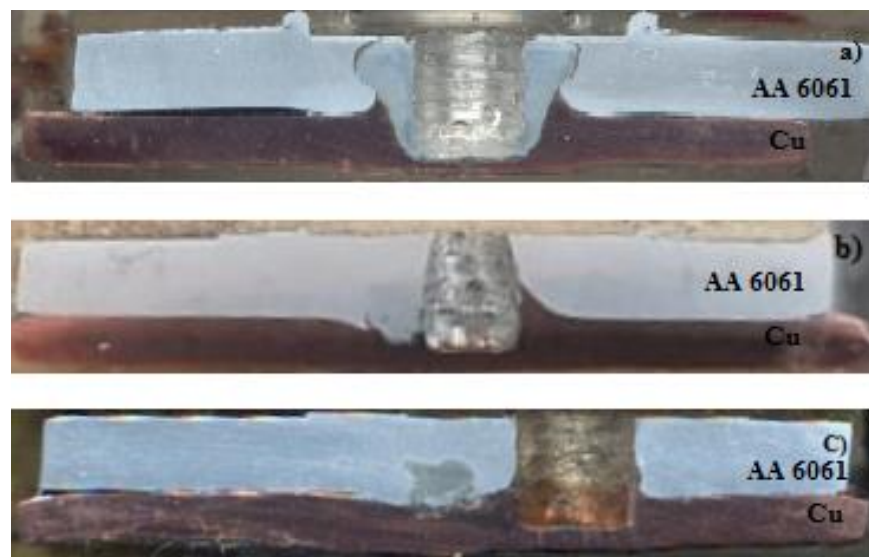travelled c) stitch fssw at 4 mm distance travelled.

Fig. 18. Macro-structure of specimen at 2200 rpm – 0.2 mm plunge depth a) traditional
fssw b) stitch fssw at 2 mm weld distance c) stitch fssw at 4 mm weld distance.

3.5 Tensile shear load of weld specimens

AA 6061 and pure copper plates have been effectively jointed through spot lap welding.
The tensile-shear force values of the lap joints are impacted by variations in process parameters.
The highest tensile shear force, recorded at 4.18 kN, is attained with a rotational speed of 2000
rpm, a plunge depth of 0.2 mm, and a dwell time of 20 seconds. At 2000 rpm, the speed provides
enough heat for effective material mixing without excessive grain growth. The 0.2 mm plunge
depth ensures strong interlocking, and the 20-second dwell time allows thorough mixing and
recrystallization, resulting in the highest tensile shear force. In contrast, the lowest tensile shear
force, 2.01 kN, is achieved with a tool rotational speed of 2200 rpm, a plunge depth of 0.1 mm, and
a dwell time of 15 seconds. At 2200 rpm, the high speed can cause overheating, leading to grain
coarsening and reduced hardness. The shallow 0.1 mm plunge depth results in weak interlocking,
and the 15-second dwell time isn't enough to offset these effects, leading to the lowest tensile shear
force. **Fig. 19.** presents the variations of tensile Shear load values of welded specimens. Stress
strain curve of weld specimen of optimum shear load at rotational speed of 2000 rpm, a plunge
depth of 0.2 mm, and a dwell time of 20 seconds is recorded in **Fig. 20. Table 4** records the values
of tensile shear load and microhardness of SZ of welded specimens. Prasomthong et al. [49]

informed that the shear force values in dissimilar welding processes between Ti-4V-6Al titanium alloys and Al5052 aluminum alloy were significantly influenced by the friction stir spot welding (FSSW) parameters. Their investigation highlighted the critical role of process parameters in determining the shear strength of the welded joints, providing insights into optimizing FSSW for dissimilar materials.
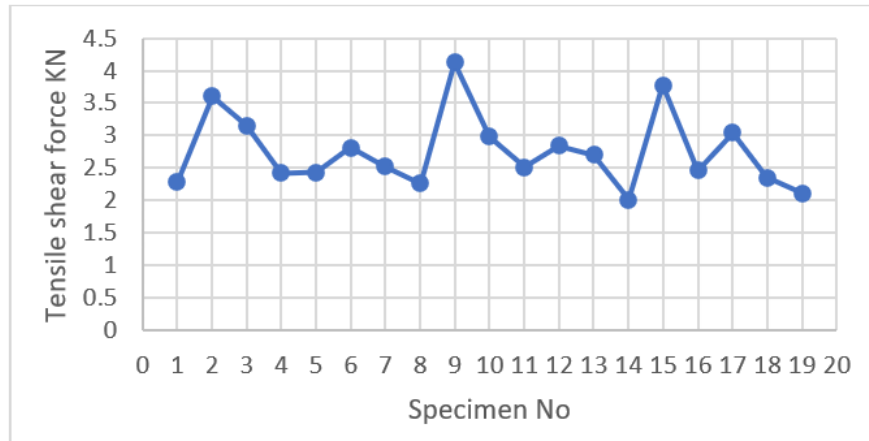

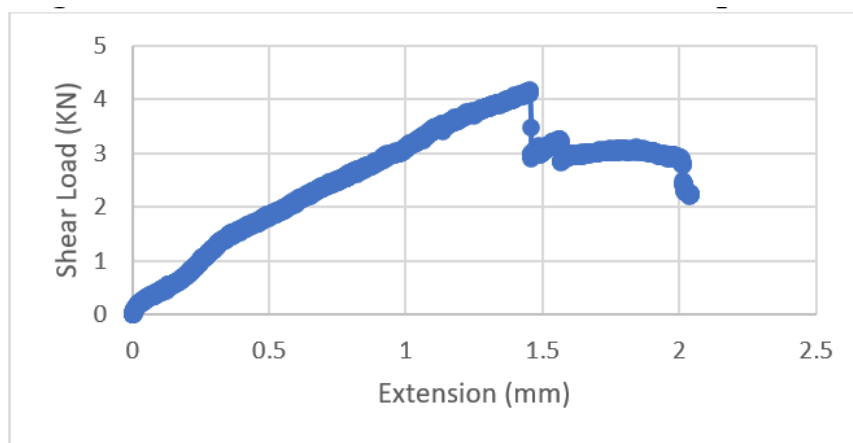**Fig. 19.** Tensile shear load values of welded specimens.

Fig. 20. Stress strain curve of weld specimen of optimum shear load at 2000rpm-20 sec -0.2mm.

3.6 Microhardness of SZ of weld specimens

The Microhardness of SZ values of the lap joints is influenced by fluctuations in process parameters. The maximum microhardness of SZ, which was measured at 122.78 HV, is obtained when utilizing a rotational speed of 2200 rpm, a plunge depth of 0.2 mm, and a dwell time of 15 seconds. The high rotational speed (2200 rpm) generates substantial heat for effective mixing, while the 0.2 mm plunge depth ensures good penetration, and the 15 second dwell time allows proper heat distribution. Together, these conditions lead to maximum microhardness. Conversely, the minimum Microhardness of SZ, at 54.1 HV, is reached by employing a tool rotational speed of 2000 rpm, a plunge depth of 0.2 mm, and a dwell time of 15 seconds. At 2000 rpm, the heat generated may be insufficient for optimal material mixing and recrystallization, potentially leading to less effective bonding and lower hardness. The combination of this lower speed with a 0.2 mm plunge depth and 15 seconds dwell time doesn't provide enough thermal energy for enhancing microhardness, resulting in the minimum observed value.The variations in the microhardness of SZ values of welded specimens are illustrated in **Fig. 21.** Silachai et al. [50] reported that the

rotational speed, dwell time, and plunge depth significantly influence the microhardness of the
stirred zone in FSSW of Al6061-T6 aluminum alloy and HSS590 high-strength steel.

Table 4. The values of tensile shear load and microhardness of SZ of welded specimens

| No	Speed Rotational	time Dwell	Depth Plunge	shear Tensile force	Microhardness of SZ (Hv)
	rpm	sec	mm	KN	
A1	1800	10	0	2.275	62.85
A2	1800	15	0	3.604167	66.025
A3	1800	20	0	3.147917	63.55
A4	1800	10	0.1	2.416667	76.425
A5	1800	15	0.1	2.427083	73.675
A6	1800	20	0.1	2.810417	83.125
A7	2000	10	0	2.521875	79.4
A8	2000	15	0.1	2.258333	95.8
A9	2000	20	0.2	4.127083	73.3
A10	2000	10	0.1	2.983333	68.3
A11	2000	15	0.2	2.504167	54.1
A12	2000	20	0	2.835417	78.6
A13	2200	10	0.1	2.704167	72.825
A14	2200	15	0.1	2.010417	61.35
A15	2200	20	0.1	3.773583	87.23
A16	2200	10	0.2	2.460417	64.2
A17	2200	15	0.2	3.041667	122.77
A18	2200	20	0.2	2.347917	79.8
A19	2000	15	0	2.11	88
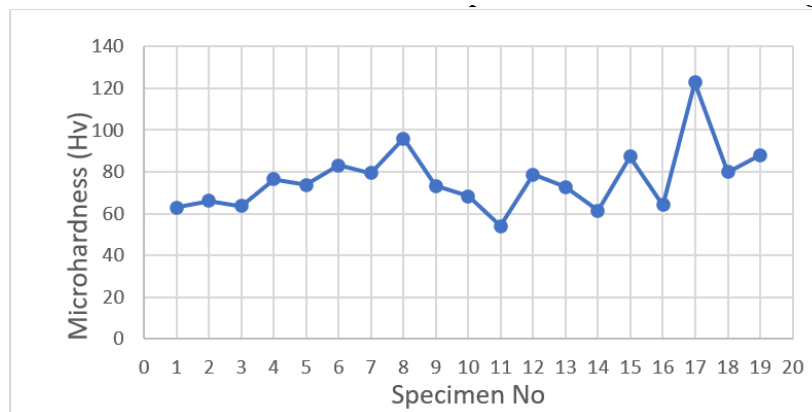
Fig. 21. Microhardness of sz values of welded specimens.

3.7 Metallurgical investigation and fracture SEM analysis

The microstructural composition of the Nugget zone is bordered by the Thermo-Mechanically Affected Zone (TMAZ) on either side, where the attainment of flawless joints is possible through the careful selection of FSSW parameters. **Fig. 22(a)**. exhibits the micro- structure of recrystallized grains in stirred zone .The equiaxed grains present in the nugget zone result from the process of churning and the recrystallization of plasticized material [51]. **Fig. 22(b)** illustrates the thermomechanically affected zone where the grains have started to recrystallize. In this region, intermetallic compounds of the β equilibrium phase of Mg_2Si appear as dispersed dark tiny particles, along with gray precipitates of Fe_3SiAl_{12}, particularly on the upper side of the TMAZ [54]. **Fig. 22(c)** presents HAZ with coarse grains due heat effect and **Fig. 22(d)** shows the elongated grains of base metal of AA 6061 base metal of AA6061. The microstructural variations observed across these zones are influenced by the distinct thermal and mechanical conditions encountered during the friction stir spot welding process. The stirred zone features an average grain size of 7.52 μm, which contrasts with the 15.7 μm grain size in the thermo-mechanically affected zone. In the heat-affected zone, the grain size averages 63.22 μm, while the base metal shows an average grain size of 38.1 μm.
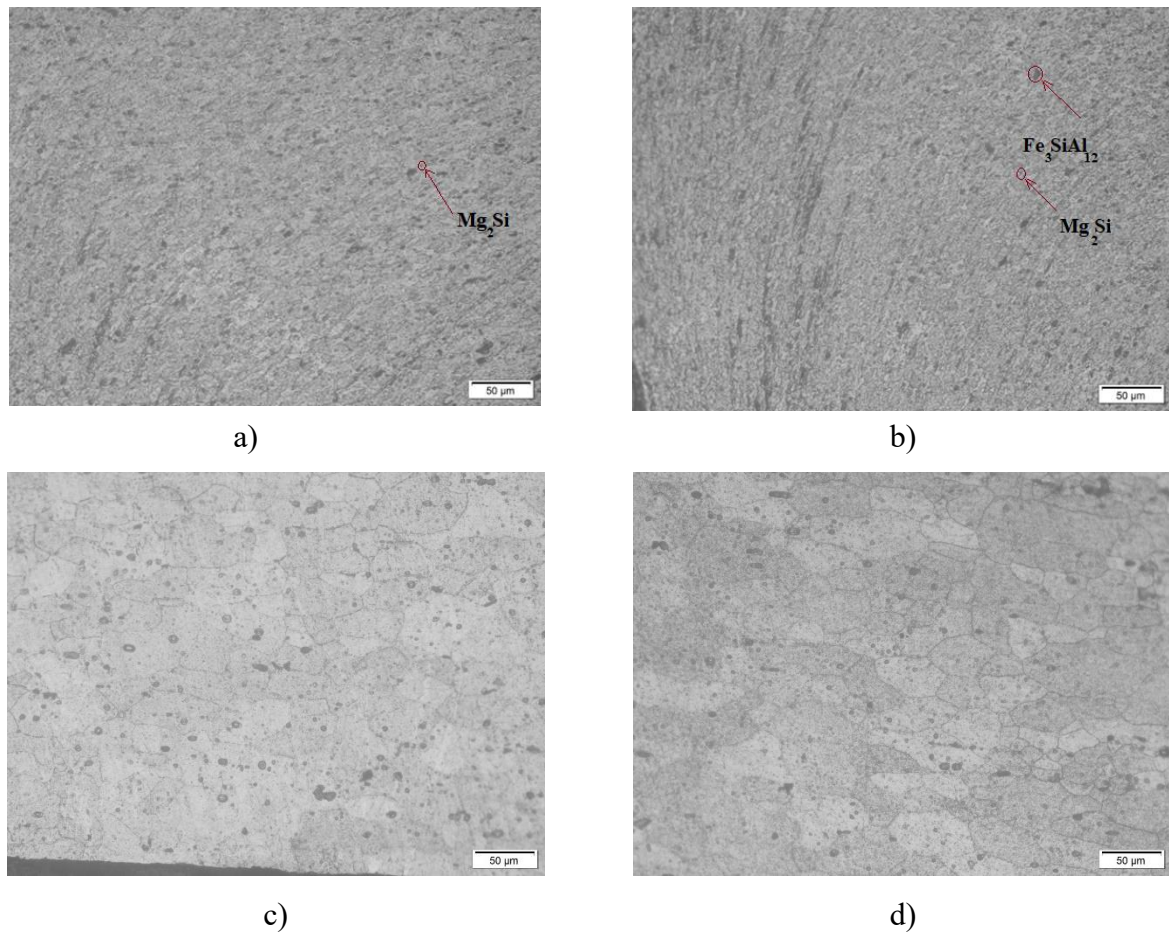
Fig 22. Micro-structure of specimen at 2200 rpm – 0.2 mm plunge depth a) SZ b) TMAZ c) HAZ
d) BM of AA6061 .

Fig 23. Micrograph of interface of AA 6061 and pure Cu of welded specimen at 2200 rpm – 0.2
mm plunge depth.

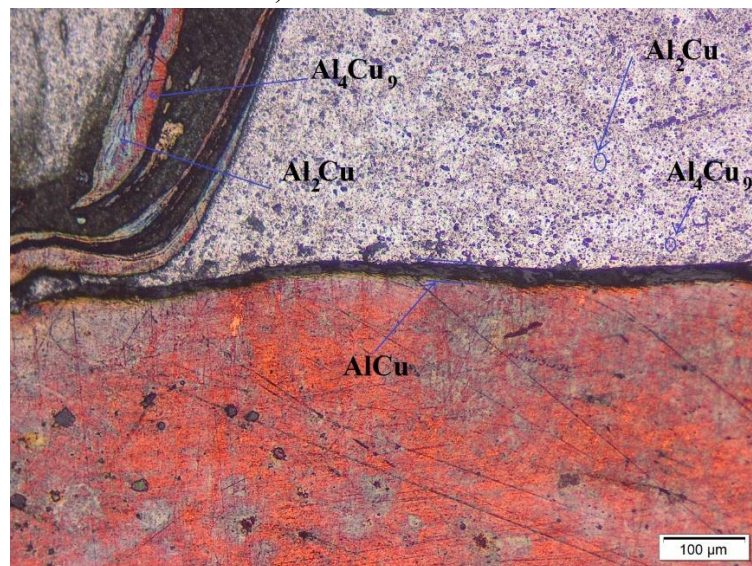**Fig. 23** shows a micrograph of interface of AA 6061 and pure Cu of welded specimen at 2200 rpm – 0.2 mm plunge depth. The micrograph reveals dispersed red-colored tiny particles and columnar shapes of the γ- Al_4Cu_9 phase, which are distinct regions within the aluminum matrix. This intermetallic compound typically forms at higher copper content and is distributed in a

somewhat dispersed manner, indicating a reaction zone where copper has diffused into the aluminum. Additionally, the θ-Al_2Cu phase is present and can be identified by its bright blue-colored tiny particles and columnar shapes at the interface. Al_2Cu is a common intermetallic compound in Al-Cu systems, known for its layered structure, which forms at slightly lower copper concentrations compared to Al_4Cu_9. Another intermetallic phase identified in the micrograph is AlCu, which forms a distinct layer of 30 µm thick at the interface between the aluminum and copper. η-AlCu phase typically exhibits a more planar or columnar morphology, indicative of solid-state diffusion and reaction during the welding process. These intermetallic phases collectively highlight the complex diffusion and reaction dynamics between aluminum and copper in the welded specimen. Garg et al. [54]reported that a thick intermetallic compound (IMC) layer was detected in dissimilar Cu-AA6061 joints that were preheated before welding. Tearing and rupture were observed in the oxide-dominated intermetallic region of Cu-AA6061 FSSW joints, whereas dimples and micro-voids were prevalent in Cu-Cu joints.
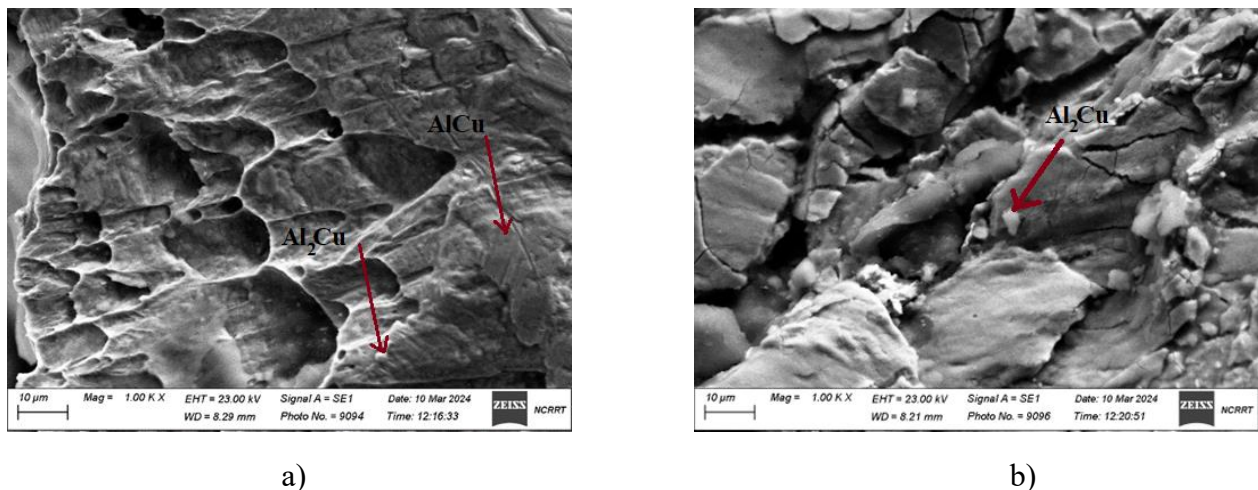

a)   b)

**Fig 24.** Fracture SEM of specimens of a) 2000 rpm – 0.2 mm – 20sec and b) 2200 rpm-0.1 mm - 15 sec.

Fig. 24(a) Shows the Fracture SEM of specimen at 2000 rpm – 0.2 mm Plunge depth – 20s dwell time. A dimpled surface, characteristic of ductile fracture, where the dimples, often exhibiting a cub shape, suggest that the material experienced significant plastic deformation before fracture. The morphology of the dimples is consistent with a ductile fracture mechanism, where microvoids form, grow, and coalesce, leading to a relatively rough fracture surface. This type of fracture is typical in materials with good ductility, such as AA 6061 aluminum alloy. **Fig. 24(b)** Shows the Fracture SEM of specimen at 2000 rpm – 0.2 mm Plunge depth – 15sec dwell time. A relatively rough surface with several cracks and fragmented regions, indicative of a brittle fracture characterized by sharp edges, cleavage-like features, and minimal plastic deformation. The fractography suggests intergranular or transgranular fracture, where cracks propagate along grain boundaries or through the grains themselves, respectively. The presence of these cracks indicates a failure mode where the material may have been subjected to high stress, leading to brittle behavior.
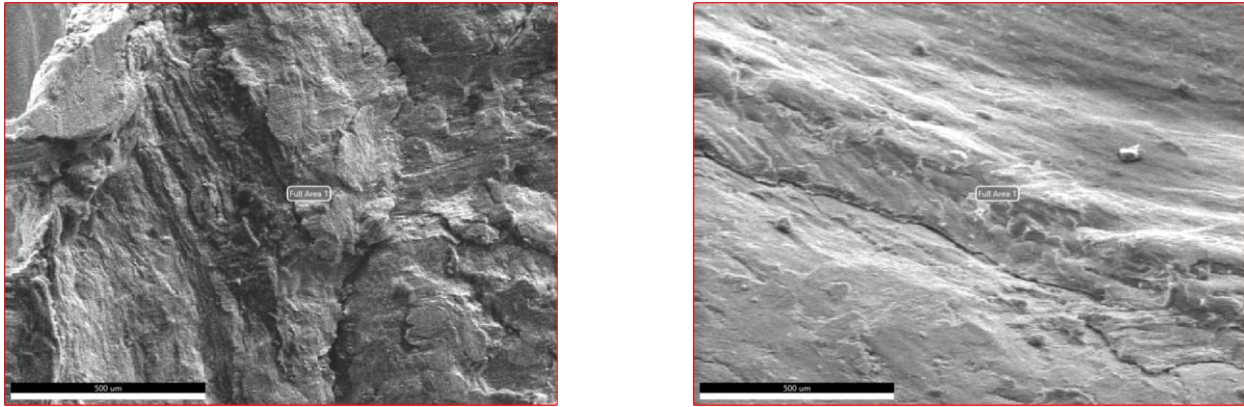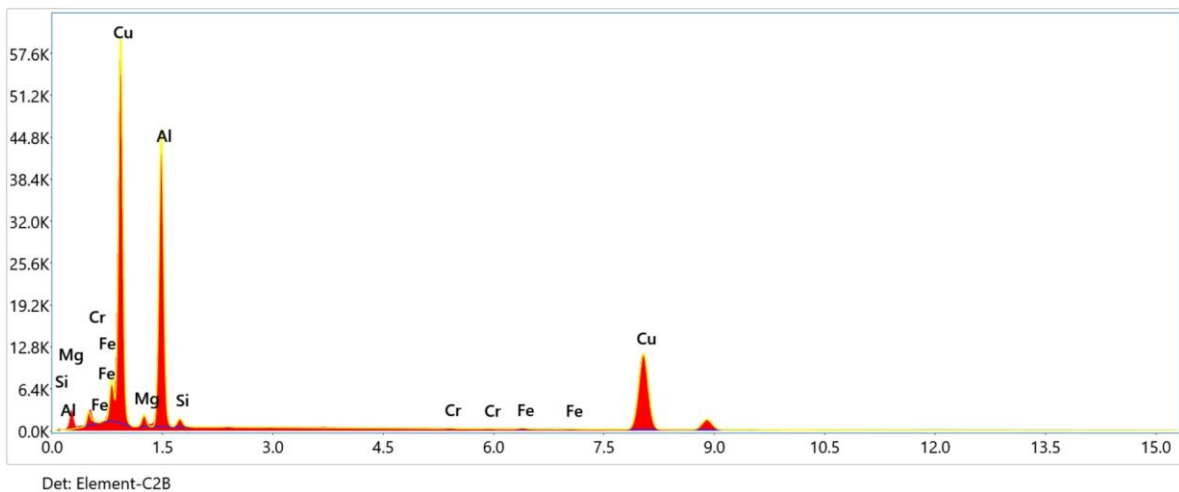
a)

b)

Fig 25. Fracture EDX of specimens at a) 2000 rpm – 0.2 mm plunge depth – 20 sec dwell time b)
2200 rpm – 0.1 mm plunge depth – 15 sec dwell time.
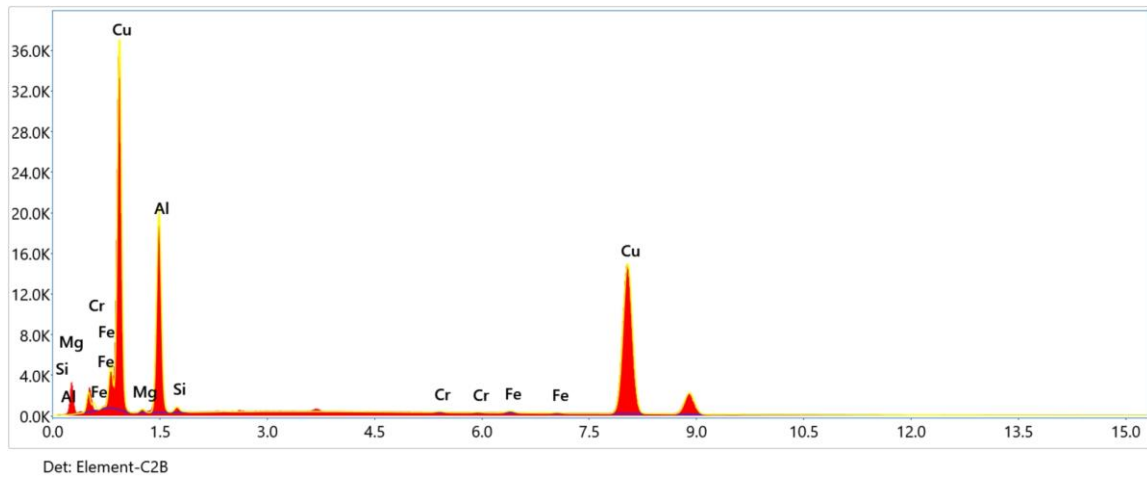
a)

b)

Fig 26. EDX analysis of welded fracture specimens at a) 2000 rpm – 0.2 mm plunge depth – 20
sec dwell time b) 2200 rpm – 0.1 mm plunge depth – 15 sec dwell time.

Table 5. Elemental analysis of fracture zone of welded sample at 2000 rpm – 0.2 mm Plunge
depth – 20 sec dwell time

Element	Weight %	Atomic %	Net Int.	Error %
MgK	0.79	1.43	45.13	15.66
AlK	31.50	51.14	2629.11	8.96
SiK	0.80	1.25	68.83	15.90
CrK	0.18	0.16	22.97	24.94
FeK	0.38	0.30	45.89	14.25
CuK	66.34	45.73	3967.20	2.00

Table 6. Elemental analysis of fracture zone of welded sample at 2200 rpm – 0.1 mm Plunge
depth – 15 sec dwell time.

Element	Weight %	Atomic %	Net Int.	Error %
MgK	2.61	3.94	230.88	10.79
AlK	49.05	66.79	5950.33	8.24
SiK	1.76	2.30	169.18	12.98
CrK	0.14	0.10	18.74	32.40
FeK	0.31	0.21	39.49	19.68
CuK	46.13	26.67	3120.59	2.05

Fig. 25(a) presents fracture EDX of specimen at 2200 rpm – 0.1 mm Plunge depth – 20sec dwell time. The surface morphology suggests a ductile fracture mode, characterized by the presence of significant plastic deformation and microvoid coalescence. The fracture surface appears rough and uneven, with ridges and valleys indicating the material's ability to absorb energy before fracturing. This rough texture is typical of ductile fractures, where the material undergoes considerable deformation. The energy-dispersive X-ray spectroscopy analysis of this region would likely reveal a homogeneous distribution of elements, suggesting minimal or controlled intermetallic formation, consistent with the ductile behavior observed. **Fig. 25(b)** presents fracture EDX of specimen at 2000 rpm – 0.1 mm Plunge depth – 15 sec dwell time. The surface morphology here suggests a brittle fracture mode, with smoother, flatter regions and the presence of sharp features indicative of cleavage. The fracture appears to have occurred with minimal plastic deformation, likely due to the higher rotational speed and shorter dwell time, which could have led to the formation of brittle intermetallic compounds or stress concentrators at the interface. The EDX analysis in this region might show a higher concentration of intermetallic phases, particularly at the interface, which would correlate with the observed brittle fracture characteristics. **Fig 26(a)**

shows EDX Analysis of welded fracture of the specimen at 2000 rpm – 0.2 mm Plunge depth – 20 sec dwell time. **Fig. 26(b)** shows EDX Analysis of welded fracture of the specimen at 2200 rpm – 0.1 mm Plunge depth – 15 sec dwell time. **Table 5** tabulates elemental analysis of Fracture zone of welded sample at the specimen at 2000 rpm – 0.2 mm Plunge depth – 20 sec dwell time. The elemental analysis at 2000 rpm with a 0.2 mm plunge depth and 20-second dwell time shows a high aluminum content (31.50% weight, 51.14% atomic) and significant copper diffusion (66.34% weight, 45.73% atomic) into the aluminum matrix. Minor elements like magnesium, silicon, chromium, and iron are present in small amounts. The combination of high aluminum and copper suggests the formation of intermetallic compounds such as Al_2Cu and possibly AlCu. The results indicate that there is a perfect mixing between Al and Cu in the joint area . **Table 6** tabulates elemental analysis of Fracture zone of welded sample at the specimen at 2200 rpm – 0.1 mm Plunge depth – 15 sec dwell time. The elemental analysis presents a substantial increase in aluminum content (49.05% weight, 66.79% atomic) and a decrease in copper content (46.13% weight, 26.67% atomic), indicating a more aluminum-rich region with less copper diffusion compared to the previous condition. Minor elements like magnesium, silicon, chromium, and iron are present in slightly higher amounts but still contribute minimally to the total composition. The higher aluminum and lower copper concentrations suggest that Al_2Cu and AlCu intermetallic compounds are more likely to form. **Fig.27** shows the binary phase diagram of Al-Cu alloys.
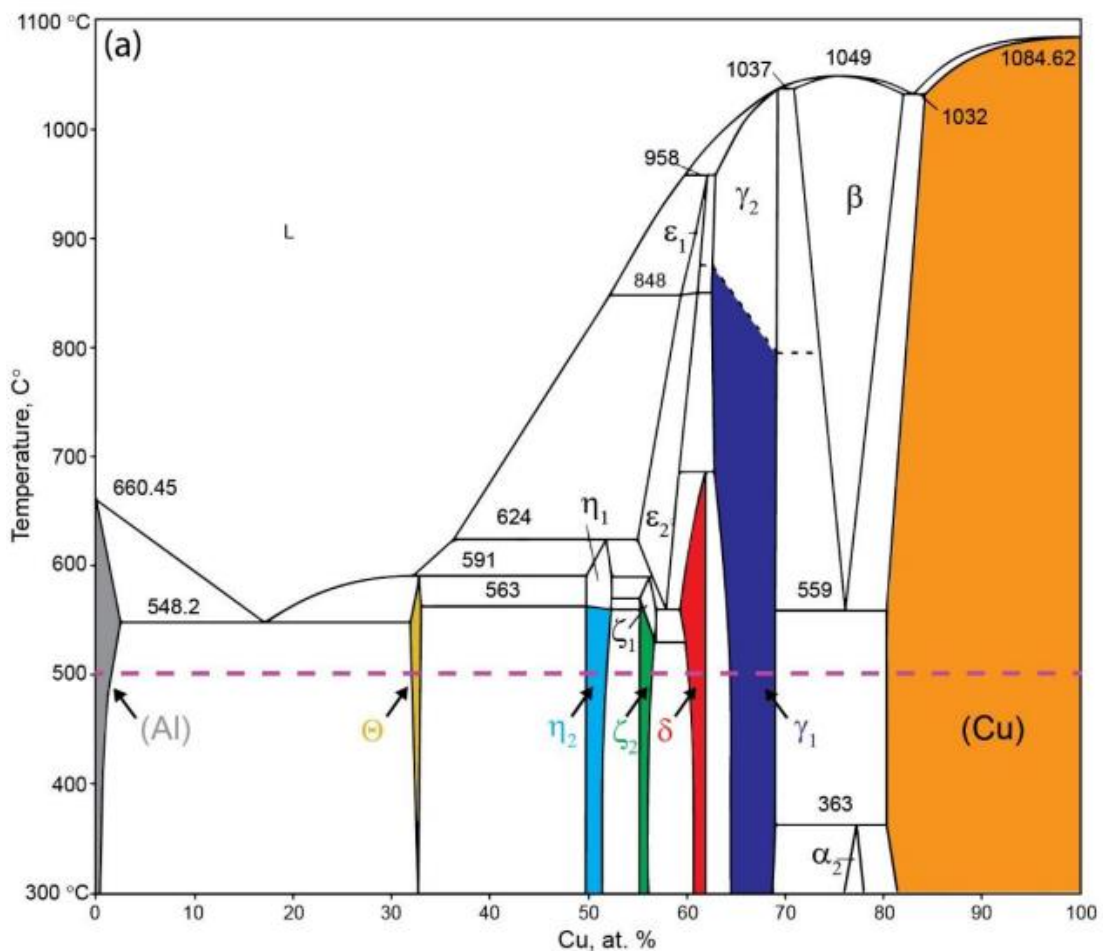

Fig 27. The binary phase diagram of Al-Cu alloys [54].

Conclusions

Based on the results obtained from the present investigation, the following conclusions can be derived:

1. At 2200 rpm tool speed and 0.2 mm plunge depth, an observation is made regarding the increase in tensile shear force. Specifically, the force rises from 2.46 KN (in traditional FSSW) to 2.64 KN (in Stitch FSSW at 2 mm distance travelled) and further to 2.68 KN (in Stitch FSSW at 4 mm distance travelled).

2. The highest shear load on lap joints of AA 6061 and pure copper welded is 4.18 KN at 2000 rpm, 20 s of dwell time, and a plunge depth of 0.2 mm while the lowest value is 2.01 KN at 2200 rpm, a plunge depth of 0.1 mm, and a dwell time of 15s .

3. The highest Microhardness value of SZ, recorded at 122.78 HV, is achieved when the rotational speed is set at 2200 rpm, the plunge depth is 0.2 mm, and the dwell time is 15 seconds. In contrast, the lowest Microhardness value of SZ, measuring 54.1 HV, is attained through the utilization of a tool rotational speed of 2000 rpm, a plunge depth of 0.2 mm, and a dwell time of 15s.

4. The analysis of the SEM images of 2000 rpm, a plunge depth of 0.2 mm, and a dwell time of 20 seconds. revealed the presence of a small number of large dimples which are indicative of ductile fracture and superior elongation characteristics.

References

[1] Smith P., Power G., 2022. High Purity Alumina – Current and Future Production. Mineral Processing and Extractive Metallurgy Review, 43(6), 747-756.

[2] ElDeeb A.B.S., Brichkin V.N., 2018. Egyptian Aluminum containing ores and prospects for their use in the production of Aluminum. Int. J. Sci. Eng. Res. 9(5), 721-731.

[3] Bray E. L., 2011. Bauxite and alumina. Min. Eng. 63(6), 44-45.

[4] Cao, S., Ma, H., Zhang, Y., Chen, X., Zhang, Y., Zhang, Y., 2013. The phase transition in Bayer red mud from China in high caustic sodium aluminate solutions. Hydrometallurgy 140, 111–119.

[5] Azof F.I., Vafeias M., Panias D. & Safarian J., 2020. The leachability of a ternary $CaO–Al_2O_3–SiO_2$ slag produced from smelting-reduction of low-grade bauxite for alumina recovery. Hydrometallurgy, 191, 105184.

[6] Stange K., Lenting C., Geisler T., 2017. Insights into the evolution of carbonate-bearing kaolin during sintering revealed by in situ hyperspectral Raman imaging. Journal of the American Ceramic Society, 101, 1–14.

[7] Erdemoğlu M., Birinci M., Uysal T., 2018. Alumina production from clay minerals: current reviews. J Polytech 21(2):387–396.

[8] Sizyakov V.M., Bazhin V. Yu., Sizyakova E.V., 2016. Feasibility study of the use of nepheline-limestone charges instead of bauxite. Metallurgist, 59, 1135–1141.

[9] Dubovikov O. A., Brichkin V. N., Ris A. D., Sundurov A. V., 2018. Thermochemical activation of hydrated aluminosilicates and its importance for alumina production. Non-ferrous Metals, 2, 3–15.

[10] Kinnarinen T., Holliday L., Häkkinen A., 2015. Dissolution of sodium, Aluminum and caustic compounds from bauxite residues. Miner Eng 79:143–151.

[11] Erdemoğlu M., Birinci M., Uysal T., Tüzer E. P., Barry T. S., 2018. Mechanical activation of pyrophyllite ore for aluminum extraction by acidic leaching. J. Mater. Sci. 53(19),13801–13,812.

[12] Sizyakov V.M., Brichkin V.N., ElDeeb A.B., Kurtenkov R.V., 2019. Egyptian Aluminum-containing Raw Materials and the Prospects for its Integrated Processing to Produce Alumina and By-products. TRAVAUX 48, Proceedings of the 37th International ICSOBA Conference and XXV Conference «Aluminium of Siberia», Krasnoyarsk, Russia, 16 – 20 September 2019.

[13] Brichkin V.N., Kurtenkov R.V., ElDeeb A.B., Bormotov I.S., 2019. State and development options for the raw material base of Aluminum in non-bauxite regions. Obogashchenie Rud 4: 31-37.

[14] España VAA, Sarkar B, Biswas B, Rusmin R, Naidu R., 2016. Environmental applications of thermally modified and acid activated clay minerals: current status of the art. Environ Technol Innov.

[15] Sadik C, El Amrani I-E, Albizane A., 2014. Recent advances in silica-alumina refractory: a review. J Asian Ceramic Soc 2(2):83–96

[16] Panda A.K., Mishra B.G., Mishra D.K., Singh R.K., 2010. Effect of sulphuric acid treatment on the physico-chemical characteristics of kaolin clay. Colloids Surf A Physicochem Eng Asp 363(1-3): 98–104.

[17] ElDeeb A.B., Brichkin V.N., Kurtenkov R.V., Bormotov I.S., 2019. Extraction of alumina from kaolin by a combination of Pyro- and hydrometallurgical Processes. Appl. Clay Sci. 172: 146-154.

[18] Pak V.I., Kirov S.S., Nalivaiko A.Y., Ozherelkov D.Y., Gromov A.A., 2019. Obtaining alumina from kaolin clay via aluminum chloride. Materials, 12, 1–12.

[19] Brichkin, V.N., Sizyakov, V.M., Vasilev, V.V., Gordyushenkov, E.E., 2013. Application of high-level calcium carbonate for synthesis products in the system $Na_2O–Al_2O_3–CaO–CO_2–H_2O$. J. Min. Inst. 202, 83–87.

[20] Sizyakov V. M., 2016. Chemical and technological mechanisms of an alkaline aluminum silicates sintering and a hydrochemical sinter processing. Journal of Mining Institute, 217, 102–112.

[21] Xu X.H., Lao X.B., Wu J.F., Zhang Y.X., Xu X.Y. & Li K., 2015. Microstructural evolution, phase transformation, and variations in physical properties of coal series kaolin powder compact during firing. Applied Clay Science, 115, 76–86.

[22] Al-Ajeel A.W.A., Abdullah S.Z., Muslim W.A., Abdulkhader M.Q., Al-Halbosy M.K., Al-Jumely F.A., 2014. Extraction of alumina from Iraqi colored kaolin by lime-sinter process. Iraqi Bulletin of Geology Mining, 10, 109–117.

[23] Aldabsheh I., Khoury H., Wastiels J., Rahier H., 2015. Dissolution behavior of Jordanian clay-rich materials in alkaline solutions for alkali activation purpose. Part I. Applied Clay Science, 115, 238–247.

[24] Sizyakov V.M., Brichkin V.N., 2018. About the role of hydrafed calcium carboaluminates in improving the technology of complex processing of nephelines. Journal of Mining Institute, 231, 292–298.

[25] ElDeeb A.B., Brichkin V.N., Sizyakov V.M., Kurtenkov R.V., 2020. Effect of sintering temperature on the alumina extraction from kaolin. Pp. 136–145 in: Advances in Raw Material Industries for Sustainable Development Goals (E. Litvinenko, editor). CRC Press, Boca Raton, FL, USA.

[26] Guo, Y., Yan, K., Cui, L., Cheng, F., Lou, H.H., 2014. Effect of Na_2CO_3 additive on the activation of coal gangue for alumina extraction. Int. J. Miner. Process. 131, 51–57. Ilic, B., Mitrović, A.A., Milicic Lj, R., 2010. Thermal treatment of kaolin clay to obtain metakaolin. Hem. Ind. 351–356 No. 64.

[27] D'Elia A., Pinto D., Eramo G., Giannossa L., Ventruti G., Laviano R., 2018. Effects of processing on the mineralogy and solubility of carbonate-rich clays for alkaline activation purpose: mechanical, thermal activation in red/ox atmosphere and their combination. Appl Clay Sci 152:9–21.

[28] Li G., Zeng J., Luo J., Liu M., Jiang T., Qiu G., 2014. Thermal transformation of pyrophyllite and alkali dissolution behavior of silicon. Appl Clay Sci 99:282–288.

[29] Birinci M., Uysal T., Erdemoğlu M., Porgalı E., Barry T., 2017. Acidic leaching of thermally activated pyrophyllite ore from Puturge (Malatya-Turkey) deposit. Proceeding of XVII Balkan Mineral Processing Congress, Antalya

[30] Habashi F., 1999. A textbook of hydrometallurgy. Métallurgie Extractive.

[31] ElDeeb A.B., Brichkin V.N., Bertau M., Awad M.E., Savinova Y.A., 2022. Enhanced alumina extraction from kaolin by thermochemical activation using charcoal. Clay Minerals 56(4), 269–283.

[32] ElDeeb A.B., Brichkin, V.N., Bertau, M., Savinova Yu. A., Kurtenkov R.V., 2020. Solid state and phase transformation mechanism of kaolin sintered with limestone for alumina extraction. Appl. Clay Sci. 196.

[33] ElDeeb A.B., Brichkin V.N., Povarov V.G., Kurtenkov R.V. 2020. The activating effect of carbon during sintering the limestone-kaolin mixture. Tsvetnye Metally 7: 18-25.

[34] ElDeeb A.B., Brichkin, V.N., Kurtenkov R.V., Bormotov I.S., 2019. Factors affecting on the extraction of alumina from kaolin ore using lime-sinter process. Pp. 502-508 in: Topical Issues of Rational Use of Natural Resources 2 (E. Litvinenko, editor). CRC Press, Boca Raton, FL, USA.

[35] Azof F.I., Yang Y., Panias D., Kolbeinsen L., Safarian J., 2019. Leaching characteristics and mechanism of the synthetic calcium-aluminate slags for alumina recovery. Hydrometallurgy, 185, 273–290.

[36] ElDeeb A.B., Brichkin V.N., Kurtenkov R.V., Bormotov I.S., 2021. Study of the peculiarities of the leaching process for self-crumbling limestone–kaolin cakes. Obogashchenie Rud, 2021, 27–32.